Supplementary information: Coherent multi-pulsing induced by engineered heterogeneity in diode laser arrays

Greggory Scranton[1], Kendall Golden[2], Olivier Spitz[1,*], Arindam Mishra[1], Igor Belykh[2,†], and Yehuda Braiman[1,3,‡]

[1]The College of Optics and Photonics (CREOL), University of Central Florida, Orlando, FL 32816, USA
[2]Department of Mathematics and Statistics and Neuroscience Institute, Georgia State University, P.O. Box 4110, Atlanta, Georgia, 30302-410, USA
[3]Department of Electrical and Computer Engineering, University of Central Florida, Orlando, FL 32816, USA
[*]olivier.spitz@ucf.edu
[†]ibelykh@gsu.edu
[‡]yehuda.braiman@ucf.edu

Single-laser dynamics with the Lang-Kobayashi models

The peculiarity of pulsing within the framework of this study is that it requires a network of emitters to be triggered. This process can be optimized with adequate engineered frequency detuning, as highlighted in the main text. Yet, our model can also be studied in the context of a single laser subject to external optical feedback, and in this case, it does not show pulsing dynamics. Details about the nonlinear dynamics that can be observed in this configuration are found in Supplementary Fig. 1, and those states are in good agreement with prior studies about the same configuration[1,2]. It is worth noting that in an array of lasers, the same dynamics can also be observed, but we focused only on the pulsing state, as it has not been reported previously. For a high bias current (seven times) above the threshold, Supplementary Fig. 1 (a) shows that the single laser exhibits a steady-state behavior up to an intermediate feedback level of 10 ns^{-1}. The corresponding unwrapped phase in Supplementary Fig. 1 (b) is monotonically decreasing and no specific feature is highlighted in the electrical spectrum of Supplementary Fig. 1 (c). Further increase of the feedback strength to 10.8 ns^{-1} triggers a first kind of switching dynamics in the output of the laser, as one can observe in Supplementary Fig. 1 (d). Switching dynamics correspond to a train of pulses, rather than the pulsing dynamics shown in the main text for arrays of lasers. Each train of pulses is composed of many pulses, and the overall behavior is periodic. As mentioned, we found no single pulsing configuration for the lone laser under external optical feedback. The typical phase behavior of switching dynamics, shown in Supplementary Fig. 1 (e), is also very different from the phase behavior during pulsing, which will be discussed in an upcoming figure. Phase increases in steps during the pulse train, then abruptly decreases outside the pulse train, with a gradual diminution over several periods. The electrical spectrum in Supplementary Fig. 1 (f) comprises several broad components of discrete peaks. The interval between these multiple peaks corresponds to the switching dynamics' repetition frequency. The oscillation frequency within the switching dynamics corresponds to the maximum of the electrical spectrum. From this feedback strength value, a slight increase tunes the switching dynamics, as visualized in Supplementary Fig. 1 (g). The laser output still shows a train of pulses, but the number of pulses in the train has increased, and the pulse amplitude is more consistent. The evolution of phase in Supplementary Fig. 1 (h) underscores that the two switching dynamics share similar features, and that confirms the difference with pulsing dynamics. The electrical spectrum shown in Supplementary Fig. 1 (i) does not differ much from that shown in Supplementary Fig. 1 (f), but each peak is broadened. A wide variety of switching dynamics (not shown here) can be obtained when varying κ^f around 11-14 ns^{-1}. As the feedback strength increases, the train of pulses grows until it becomes continuous, leaving only the fast oscillation. Such state can be observed in Supplementary Fig. 1 (j) for $\kappa^f = 17$ ns^{-1}. The phase decreases over long time scales and otherwise follows the oscillation pattern at short time scales, as seen in Supplementary Fig. 1 (k). The electrical spectrum in Supplementary Fig. 1 (l) contains the frequency component related to the oscillation frequency and several harmonics of the main frequency. Each contribution is narrow-band, in contrast to the electrical spectra for switching dynamics. In this single-laser configuration, intermediate feedback strength can also lead to low-complexity chaos dynamics, and this is illustrated in Supplementary Fig. 1 (m) for $\kappa^f = 25$ ns^{-1}. The phase in Supplementary Fig. 1 (n) now decreases much faster with time and shows small amplitude fluctuations that seem to retain an almost periodic behavior with a typical scale close to round-trip time (3 ns). The electrical spectrum in Supplementary Fig. 1 (o) displays a wide component, which is a typical feature of chaos dynamics, but discrete

peaks can still be found within the structure, hence explaining why the temporal pattern of Supplementary Fig. 1 (m) belongs to low-complexity chaos.

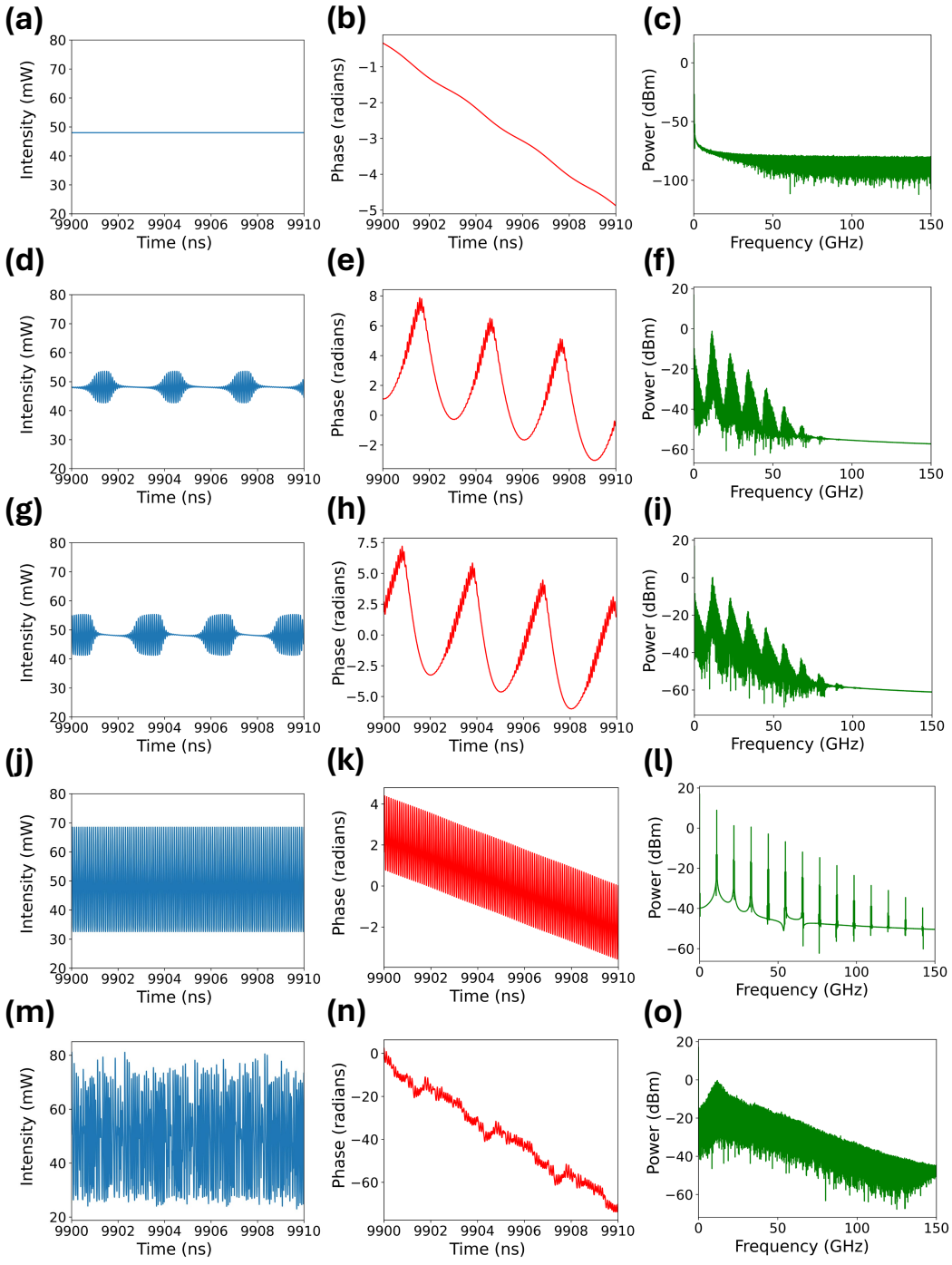

Supplementary figure 1. Nonlinear dynamics that can be observed for a bias current high above threshold ($\beta = 7$) and several conditions of feedback strength in a single laser; (a) Intensity time trace, (b) phase time trace, and (c) electrical spectrum for $\kappa^f = 10$ ns^{-1}, illustrating steady-state dynamics at low feedback strength; (d-f) identical to (a-c) but for $\kappa^f = 10.8$ ns^{-1}, corresponding to a first type of switching dynamics; (g-i) identical to (a-c) but for $\kappa^f = 11$ ns^{-1}, corresponding to a second type of switching dynamics; (j-l) identical to (a-c) but for $\kappa^f = 17$ ns^{-1}, corresponding to fast oscillations in the output of the laser; (m-o) identical to (a-c) but for $\kappa^f = 25$ ns^{-1}, corresponding to low-complexity chaos dynamics. The frequency detuning for this laser is 0. Other parameters not mentioned here are as shown in Supplementary Table 1.

Default parameters for the Lang-Kobayashi model simulations

The Lang-Kobayashi model in the context of an array of semiconductor lasers takes into account various dynamical parameters that we list in this section, and the values for each parameter used in the 30 laser models of the main text are gathered in Supplementary Table 1. The relationship between the threshold current J_{th}, defined as a number of electrons per unit of time (used in the equations) and I_{th}, the threshold current in unit of A (described in the table) is $J_{th} = \frac{I_{th}}{e}$, with e the charge of an electron. The external cavity time delay is held constant across all lasers in the simulations presented. While we also computationally verified the persistence of pulsing dynamics in the presence of disordered time delays, we focus here on non-disordered configurations to better elucidate the underlying mechanism and facilitate comparison with the reduced models. Supplementary Table 2 lists the frequency detuning parameters used in the 30-laser Lang-Kobayashi model, corresponding to the simulation results presented in Supplementary Fig. 2. This is similar to the 30 laser model mentioned in the main text, but with the addition of random variation in the frequency detuning values. Supplementary Table 3 shows the parameters used in the two-laser Lang-Kobayashi model, whose simulation results are shown in Fig. 4(a) in the main text.

Supplementary table 1. Details of the parameters for simulating the 30-Lang-Kobayashi laser model array. The values used in the simulations are compatible with those usually found in semiconductor lasers.[3,4]

Symbol	Description	Value
λ	Wavelength	770 nm
α	Linewidth enhancement factor	5.0
g	Differential gain coefficient	1.5×10^{-5} ns^{-1}
s	Gain saturation coefficient	2×10^{-7}
γ	Cavity loss	500 ns^{-1}
N_0	Carrier number at transparency	1.5×10^{8}
γ_n	Carrier loss rate	0.5 ns^{-1}
$f_{odd} = \omega_{odd}/2\pi$	Frequency detuning for odd lasers	-2 GHz
$f_{even} = \omega_{even}/2\pi$	Frequency detuning for even lasers	2 GHz
τ	Feedback delay time	3 ns
κ^f	Feedback strength	varied
d	Cross-laser reinjection efficiency	0.75
β	Pump factor	7.0
I_{th}	Threshold pump current for a single laser	14.7 mA

Perturbation of the frequency detuning in the 30-laser configuration

The main text details the pulsing dynamics in an array of 30 lasers with frequency detuning. To optimize the pulsing dynamics, which includes the juxtaposition of anti-phase and in-phase synchrony, we focused on a configuration with a frequency detuning of -2 GHz for odd lasers and 2 GHz for even lasers. However, this requirement can be relaxed without significantly impacting the observed dynamics. With the frequency detuning values listed in Supplementary Tab. 2, one can observe the pulsing dynamics displayed in Supplementary Fig. 2, among others. A configuration with a single pulse per period is illustrated in Supplementary Fig. 2 (a) for the full array of 30 lasers, and the alternate behavior between the even and the odd lasers is still observed. In Supplementary Fig. 2 (b) the phase time trace for an even and an odd laser shows that the phase behavior strongly differs compared to what was described in Supplementary Fig. 1 for a single laser. The phase is overall decreasing, and there is a positive step for the even lasers and a negative step for the odd lasers each time a pulse is triggered. The synchrony behavior is detailed in Supplementary Fig. 2 (c) and shows again that anti-phase synchrony is followed by in-phase synchrony. Pulsing in the odd lasers aligns with the anti-phase behavior, while pulsing in the even lasers coincides with the in-phase behavior. We also highlight a case with two pulses per period, as seen in Supplementary Fig. 2 (d). The phase time trace in Supplementary Fig. 2 (e) confirms that the number of steps is related to the number of pulses, as two steps per period can be observed. The last panel, Supplementary Fig. 2 (f), showcases the synchrony features already observed, without the perturbation of frequency detuning. Overall, this example underscores that the frequency detuning does not need to be strictly -2 or 2 GHz to observe pulsing, and an uncertainty of more than 0.1 GHz can be tolerated for some lasers in the array. This finding is noteworthy because it can be difficult to experimentally fabricate an array of lasers with extremely precise frequency detuning. A typical uncertainty of 0.1 GHz can be achieved more realistically and should not impact the pulsing phenomenon. This alternating configuration of detuning values was designed to encourage pulsing; however, pulsing can also be achieved with other non-alternating

Supplementary table 2. Frequency detuning values for the 30-laser array in the perturbed detuning case.

Laser number	Frequency detuning (GHz)
1	-2.059
2	2.008
3	-2.079
4	1.887
5	-1.998
6	2.117
7	-2.041
8	2.035
9	-1.930
10	2.008
11	-1.952
12	2.155
13	-1.781
14	2.020
15	-2.178
16	2.033
17	-1.982
18	1.893
19	-1.998
20	2.032
21	-1.883
22	2.011
23	-2.108
24	2.128
25	-2.016
26	2.068
27	-1.978
28	2.072
29	-2.028
30	2.017

configurations, as demonstrated in the next section.

Example with sparse frequency detuning configuration

In addition to the perturbed frequency detuning that is underscored in the previous section, pulsing was achieved in an example with a non-alternating detuning configuration. This example has an array of 20 lasers, and its behavior is illustrated in Supplementary Fig. 3. The frequency detuning on lasers 5, 10, and 15 is 4 GHz. All other lasers have a detuning of zero. Other parameters are the same as those shown in Supplementary Tab. 1. Pulsing has the greatest amplitude on the three lasers with 4 GHz detuning. The amplitude of the pulses is weaker for lasers farther from these detuned lasers, with the lasers on the edges showing the lowest amplitude pulses. This further proves that pulsing is driven by differences in frequency detuning between lasers in an array. The synchrony behavior shows anti-phase synchrony followed by in-phase synchrony, as seen in Supplementary Fig. 3(c) and (f), although neither is as pronounced as in the alternating-detuning cases.

Robustness against perturbations in feedback coupling for a 10-laser array

The main text analyzes pulsing dynamics in arrays with coupling coefficients given by $A_{qj} = d^{|q-j|}$ in Eq. (1), where $d \in (0,1)$ controls the exponential decay of coupling with distance. However, in experimentally fabricated laser arrays, imperfections such as angular misalignment and wavefront distortions from external mirror reflections can lead to spatially randomized, potentially nonuniform feedback. To assess the robustness of the pulsing regime under such perturbations, we introduce random

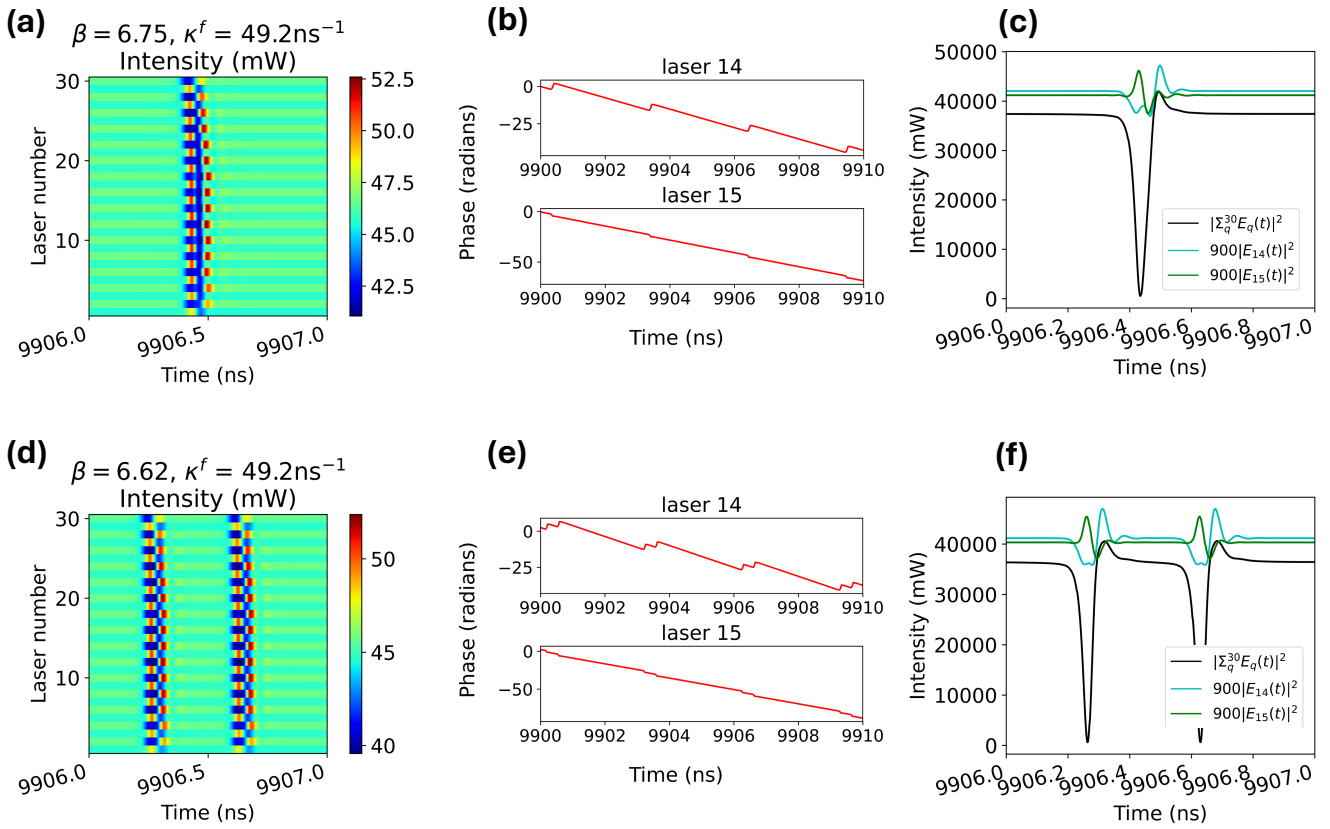

Supplementary figure 2. Robustness of pulsing dynamics in a 30-laser array under perturbed frequency detuning. Investigation of a 30-laser pulsing case similar to the one highlighted in the main text, but with the addition of perturbed frequency detuning. (a) Single-pulsing dynamics in the array of 30 lasers, with the odd and even-numbered lasers showing alternate behaviors. (b) Phase time traces for one selected odd-numbered laser and one selected even-numbered laser, both showing a sharp phase step at the instant of pulsing that contrasts with the otherwise linear evolution of the phase. (c) Combined field intensity (black curve) of the 30 lasers in the array, illustrating when the lasers are anti-phase synchronized and in-phase synchronized. Also shown are the magnified intensities of an odd-numbered laser (green curve) and an even-numbered laser (cyan curve). (d-f) Same as panels (a-c) but for a configuration with two pulses per period.

variations in the coupling coefficients. Specifically, we modify the coupling matrix to include emitter-specific deviations:

$$A_{qj} = d^{|q-j|} d_r,$$

where d_r is sampled independently for each pair from a uniform distribution in the range $[0.75, 1.0]$. Supplementary Fig. 4(a) shows the original coupling matrix used in the main analysis, while Fig. 4(b) displays its perturbed version incorporating random variations. Selected simulation results for the 10-laser configuration with this perturbed coupling matrix are shown in Supplementary Fig. 5. Despite the introduced disorder, the array continues to exhibit coherent pulsing dynamics, demonstrating the robustness of the multi-pulse regime to moderate spatial perturbations in coupling.

Smile effect and pulsing robustness

To evaluate the impact of fabrication-induced smile distortions, we introduce spatial tapering in the coupling matrix of the original model in the main text. The modified coupling coefficients are defined as

$$A_{qj} = \begin{cases} d^{|q-j|} d_s^{|q-\frac{Q}{2}|} d_s^{|j-\frac{Q}{2}|}, & q \neq j, \\ 1, & q = j, \end{cases} \tag{1}$$

where $d_s \in (0, 1)$ models the reduction in coupling strength caused by the smile effect. Two representative cases are considered: a mild distortion with $d_s = 0.925$ and a stronger distortion with $d_s = 0.85$. As shown in Supplementary Fig. 4(c)-(d), these choices produce progressively tapered coupling profiles.

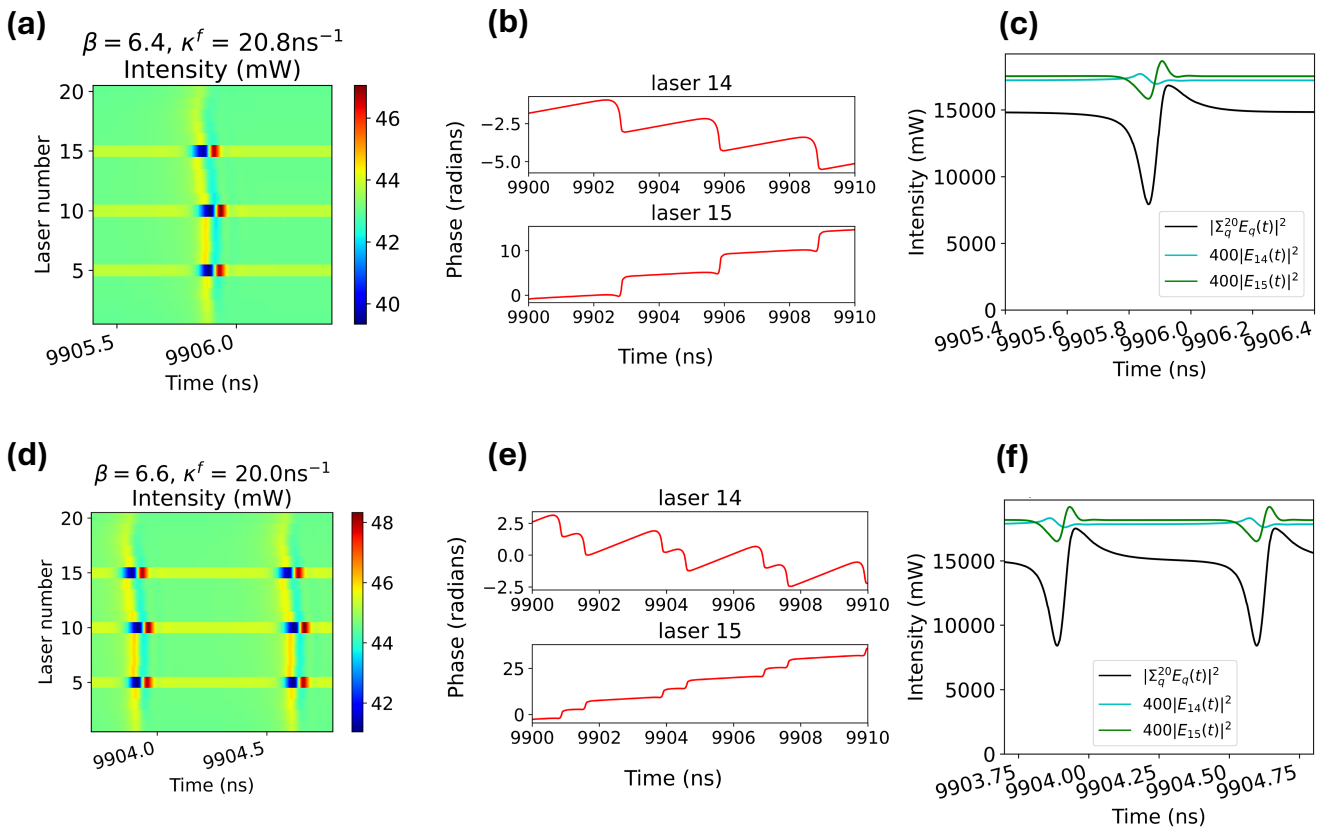

Supplementary figure 3. Investigation of a 20-laser pulsing case when a limited number of emitters in the array exhibit frequency detuning, with only $\omega_5 = \omega_{10} = \omega_{15} = 4$ GHz being non-zero. (a) Overview of single pulsing in the array of 20 lasers. (b) Phase time trace for laser #14 and laser #15, both showing a step at the instant of pulsing that contrasts with the otherwise linear evolution of the phase. (c) Combined field intensity (black curve) of the 20 lasers in the array, illustrating when the lasers are anti-phase synchronized and in-phase synchronized. This panel also shows the intensities of lasers #14 (cyan curve) and of laser #15 (green curve). (d-f) similar to (a-c) but for a configuration with two pulses per period.

Simulation results for both scenarios demonstrate that coherent pulsing persists despite the coupling asymmetry (Supplementary Figs. 6-7). For the mild smile distortion (Supplementary Fig. 6), multi-pulsing remains well synchronized across the array. For the stronger distortion (Supplementary Fig. 7), the pulsing pattern begins to degrade: edge lasers exhibit weaker coupling to the rest of the array and consequently may produce a different number of pulses per period than central lasers.

These simulations show that the core pulsing mechanism is robust to experimentally realistic levels of smile-induced nonuniformity. However, significant tapering can lead to reduced synchrony and pulse count variations near the array boundaries.

Robustness to feedback strength variations

To evaluate the robustness of pulse generation under slowly varying feedback strength, we simulate a 30-laser array with all parameters fixed (see Supplementary Table 1), except for κ^f, which is incrementally varied. Starting from a baseline value of $\kappa^f = 44.8$ ns^{-1}, where a stable single-pulse regime is observed, we gradually increase κ^f to 45.0 ns^{-1} in steps of 0.01 ns^{-1}. Notably, the simulations are conducted continuously: the final state of each run is used as the initial condition for the next, preserving temporal continuity and allowing potential multistability to manifest.

Supplementary Figure 8 shows selected time traces from this sequence. For most feedback strength values, the system remains in the single-pulse regime. However, intermittent transitions to neighboring pulsing states are observed, consistent with multistability inherent in the coupled system. These results confirm that coherent pulsing persists despite slow parameter drift, further demonstrating the robustness of the pulsing mechanism to experimental imperfections in feedback strength.

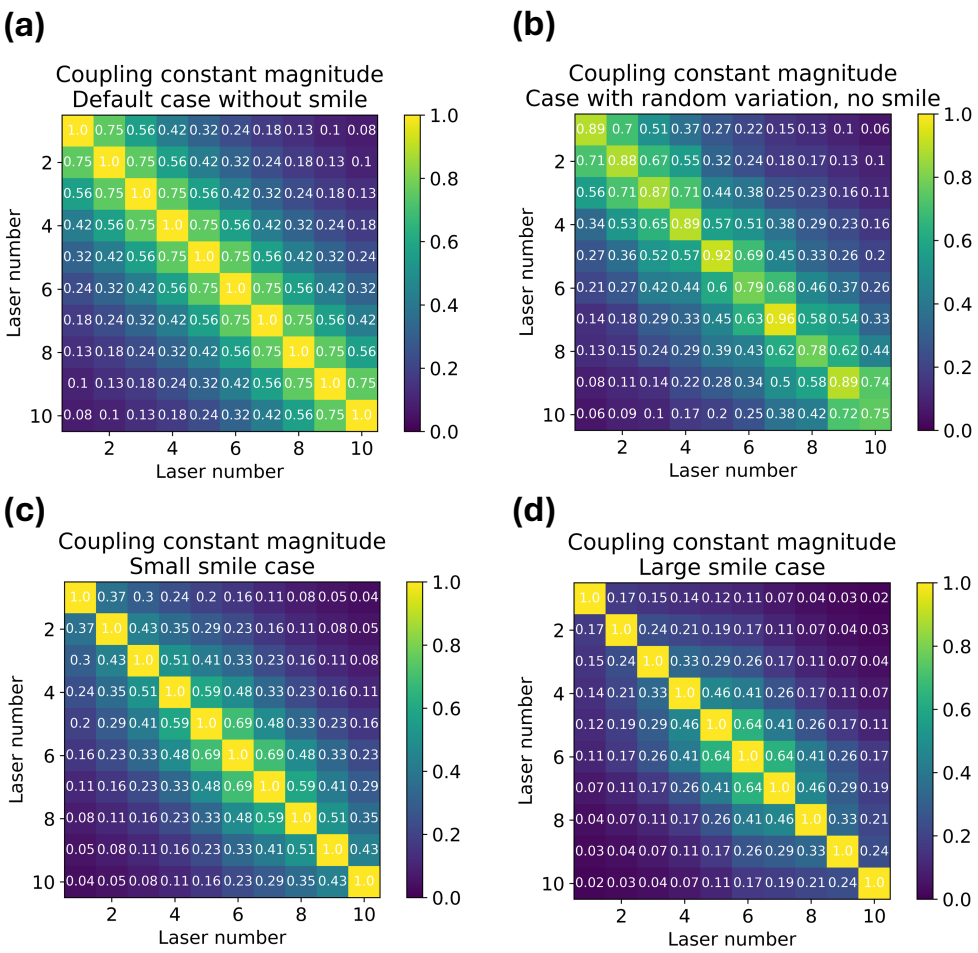

Supplementary figure 4. Coupling coefficient matrices for the different configurations considered. (a) Baseline coupling matrix used in the main analysis. (b) Coupling matrix with random variations, defined by $A_{qj} = d^{|q-j|}d_r$, where each d_r is drawn from a uniform distribution on $[0.75, 1.0]$. (c) Coupling matrix incorporating a mild smile effect, as given by Eq. (1) with $d_s = 0.925$. (d) Same as in (c), but with a stronger smile effect corresponding to $d_s = 0.85$.

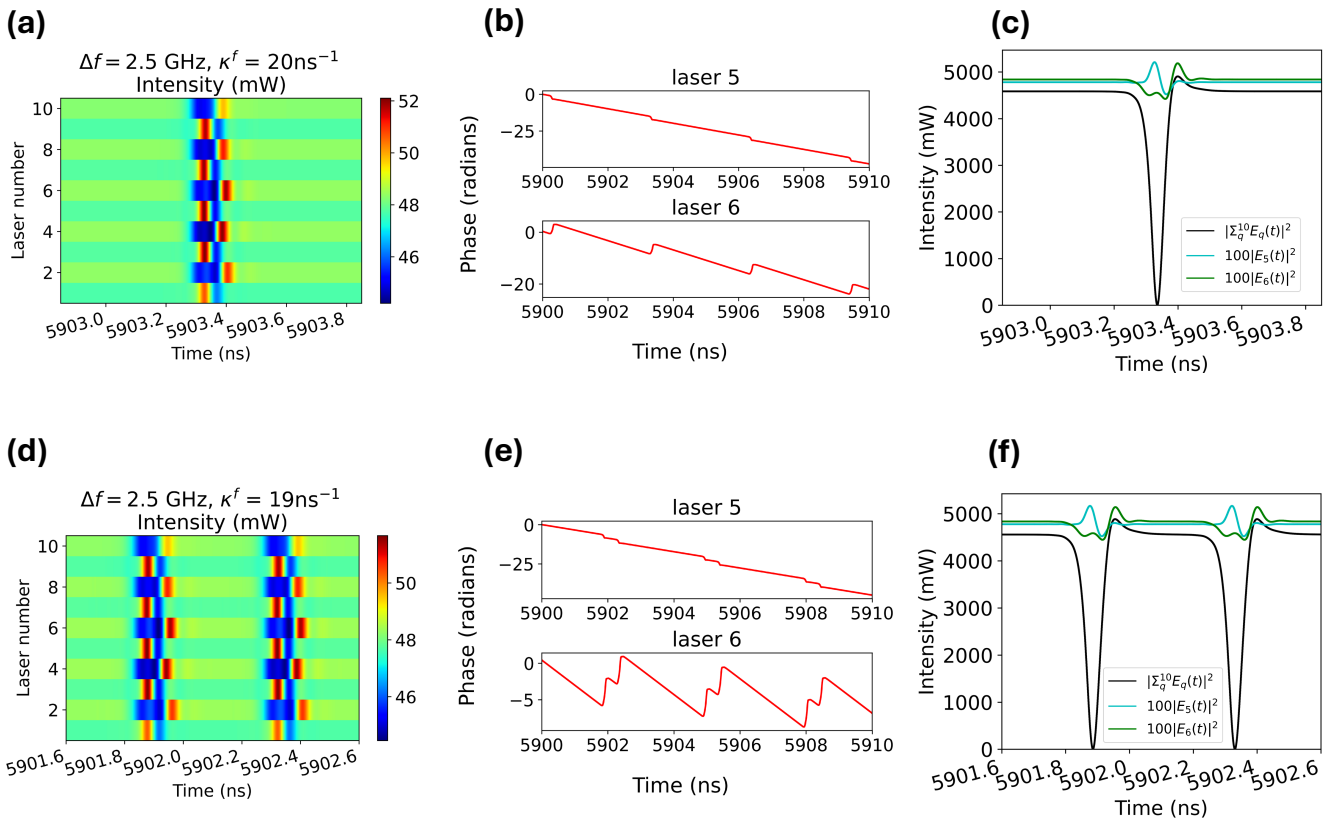

Supplementary figure 5. Robustness of pulsing dynamics in a 10-laser array with random perturbations in coupling coefficients. This configuration is analogous to the 30-laser case discussed in the main text, but with different values of Δf, κ^f, and coupling coefficients as defined in Supplementary Fig. 4(b). (a) Single-pulse dynamics for the 10-laser array, with odd- and even-numbered lasers exhibiting alternating behavior. (b) Phase traces for a representative odd-numbered and even-numbered laser, both showing abrupt phase slips at the moment of pulsing, contrasting with their otherwise linear phase evolution. (c) Combined field intensity (black curve) of the entire array, highlighting transitions between in-phase and anti-phase synchronization. The magnified intensities of a selected odd-numbered laser (cyan) and even-numbered laser (green) are also shown. (d–f) Corresponding plots for a two-pulse-per-period regime, demonstrating the persistence of robust pulsing despite coupling perturbations.

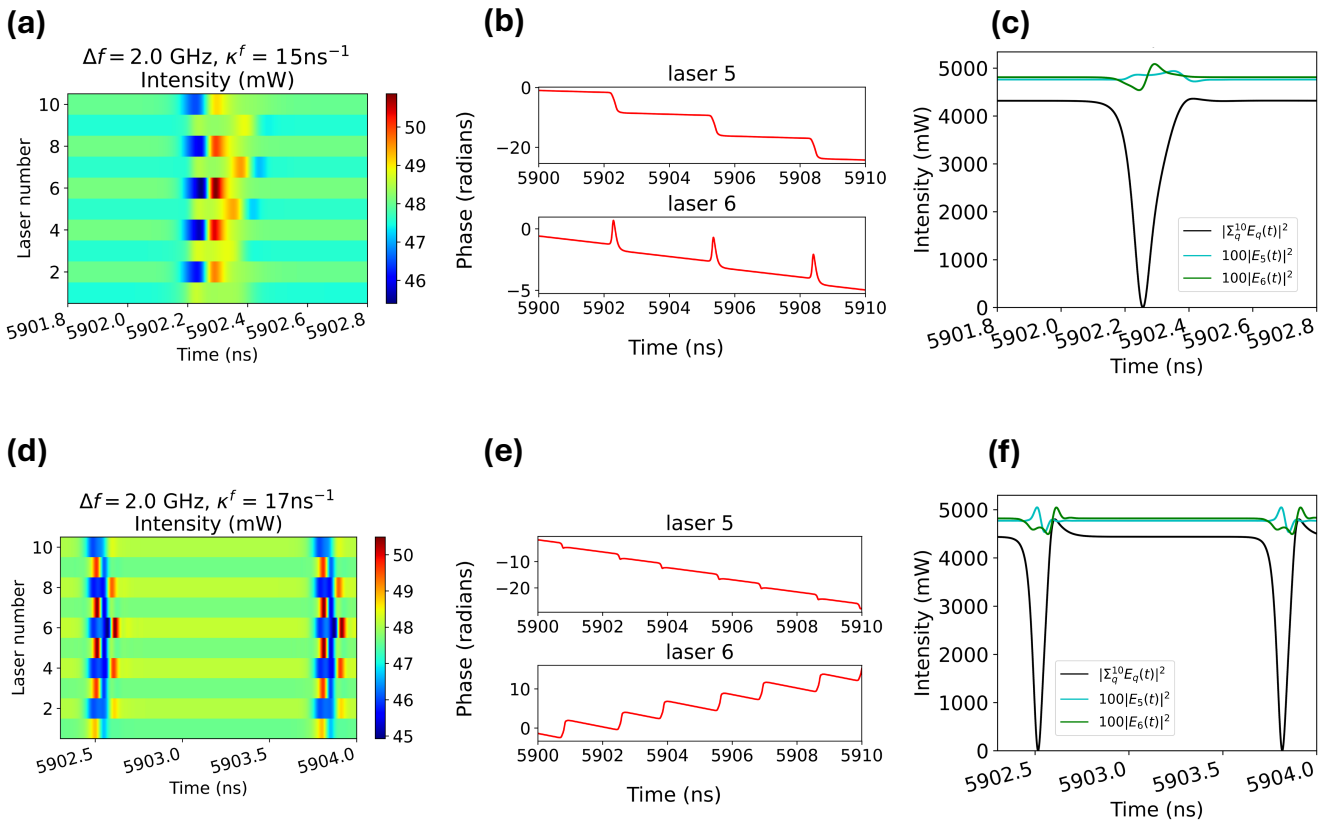

Supplementary figure 6. Mild smile effect: robustness of pulsing dynamics in a 10-laser array with coupling coefficients modified to model a mild smile effect ($g_s = 0.925$). This configuration is analogous to the 30-laser case discussed in the main text, but uses different values of Δf, κ^f, and the tapered coupling matrix shown in Supplementary Fig. 4(c). (a) Single-pulse dynamics in the 10-laser array, with odd- and even-numbered lasers exhibiting alternating pulsing behavior. (b) Phase traces for a representative odd-numbered and even-numbered laser, each showing a sharp phase slip at the instant of pulsing, in contrast to the otherwise linear phase evolution. (c) Combined field intensity (black curve) of the whole array, highlighting intervals of anti-phase and in-phase synchronization. Magnified intensity traces for a selected odd-numbered laser (cyan) and even-numbered laser (green) are also shown. (d-f) Same diagnostics as in panels (a-c), but for a regime exhibiting two pulses per period.

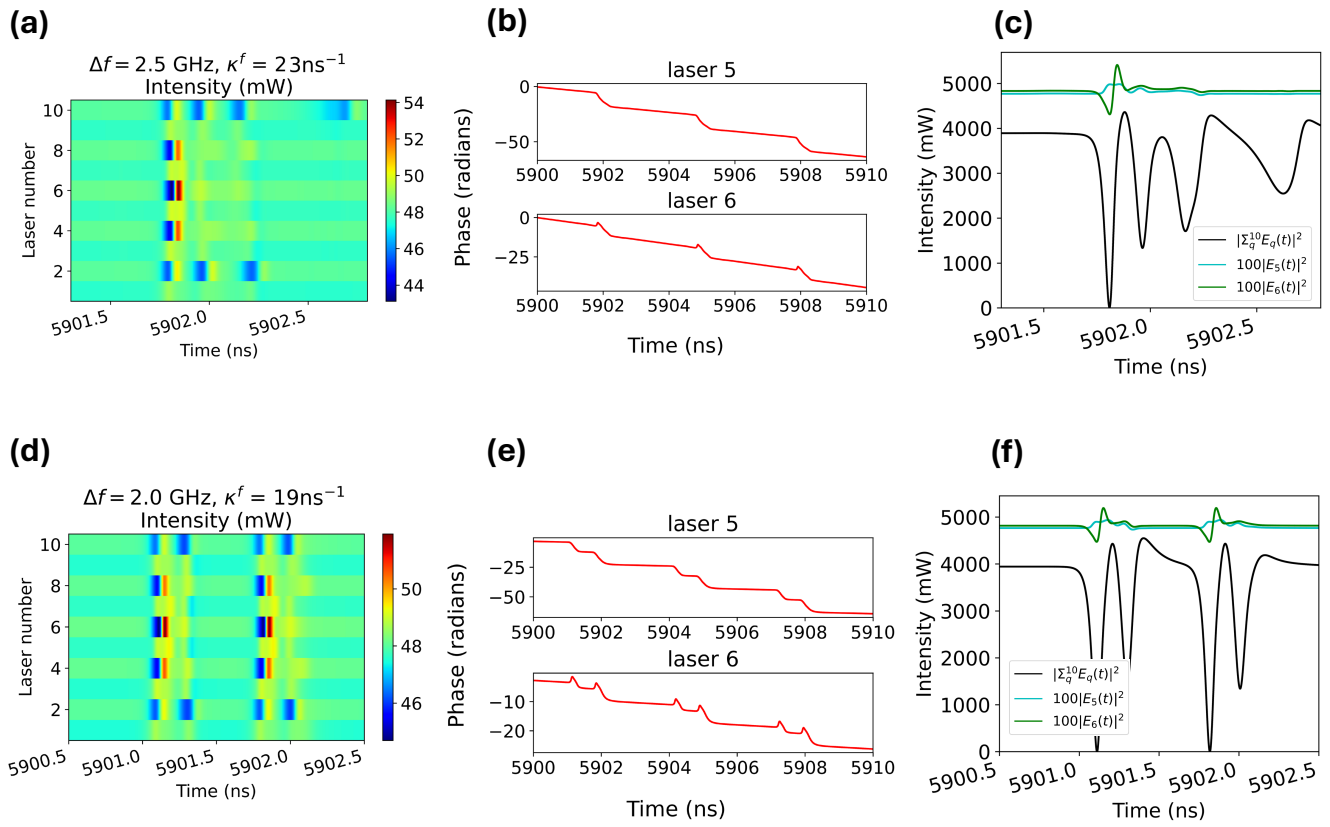

Supplementary figure 7. Stronger smile effect: robustness and partial degradation of pulsing dynamics in a 10-laser array with pronounced smile distortion ($d_s = 0.85$). This configuration mirrors the 30-laser case discussed in the main text, with distinct Δf and κ^f parameters and coupling coefficients shown in Supplementary Fig. 4(d). (a) Single-pulse dynamics across the array, with odd- and even-numbered lasers pulsing alternately. (b) Phase time traces of a representative odd-numbered and even-numbered laser, both exhibiting sharp phase slips at pulse emission, interspersed with linear phase evolution. (c) Combined field intensity (black curve) showing synchronization patterns, along with individual intensities from an odd-numbered laser (cyan) and an even-numbered laser (green). (d-f) Same as (a-c), but for a two-pulse-per-period regime. Despite the smile-induced asymmetry, coherent pulsing persists, though edge lasers exhibit altered pulse counts and reduced synchrony due to weakened coupling.

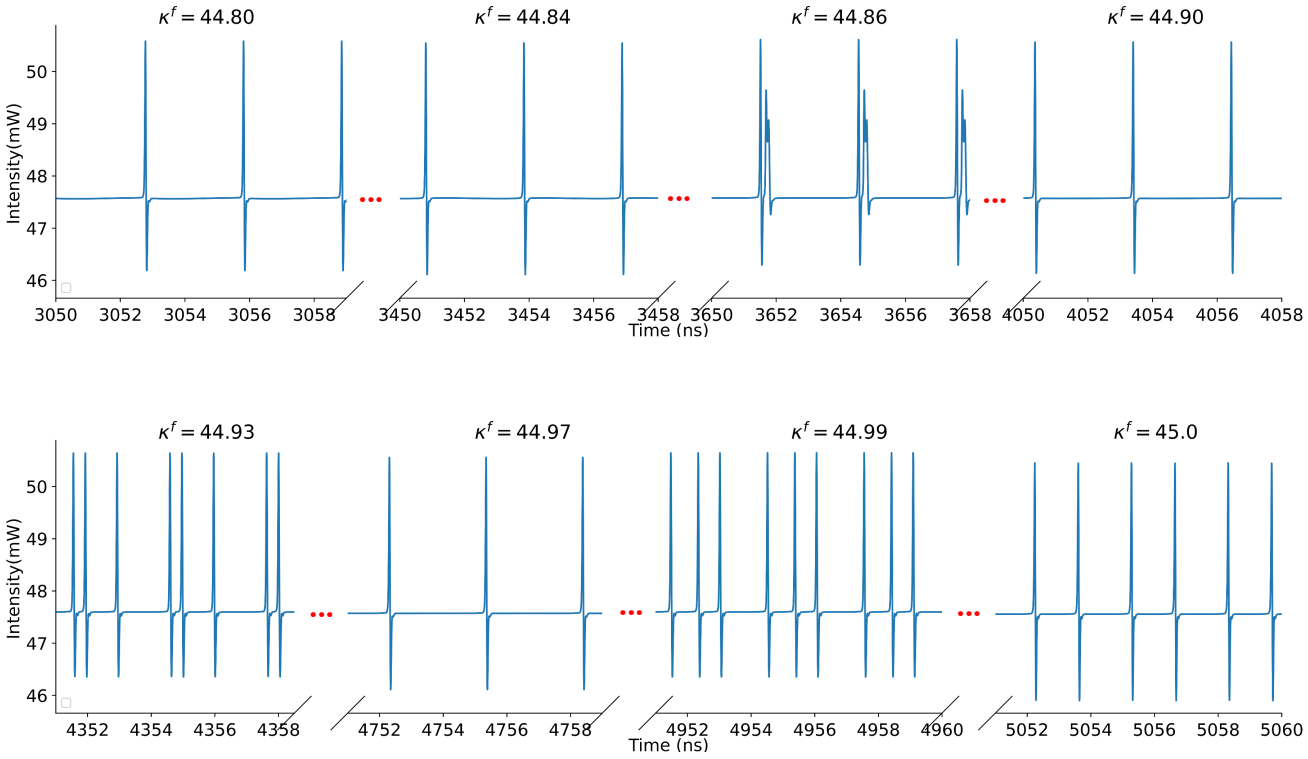

Supplementary figure 8. Zoomed-in time traces of the field amplitude for selected values of the feedback strength κ^f obtained from a continuous simulation. The feedback strength is slowly varied from 44.8 ns^{-1} to 45.0 ns^{-1} in increments of 0.01 ns^{-1}, with each simulation initialized from the final state of the previous one. For most values of κ^f, the system maintains a stable single-pulse solution. Occasional transitions to neighboring pulsing states occur due to the inherent multistability of the coupled laser array.

Robustness to Noise

To assess the impact of noise such as that introduced by thermal fluctuations or spontaneous emission, we extend the Lang–Kobayashi model from the main text by incorporating additive stochastic terms. Specifically, we consider an array of Q delay-coupled semiconductor lasers with decaying nonlocal coupling, as described in Eq. (1) of the main text, modified as follows:

$$\begin{aligned}\dot{E}_q(t) &= \frac{1+i\alpha}{2}\left(g\frac{N_q(t)-N_0}{1+s|E_q(t)|^2}-\gamma\right)E_q(t)+i\omega_q E_q(t)+\frac{\kappa^f}{Q}\sum_{j=1}^{Q}A_{qj}E_j(t-\tau)+F_{E_q},\\ \dot{N}_q(t) &= \beta J_{th}-\gamma_n N_q(t)-g\frac{N_q(t)-N_0}{1+s|E_q(t)|^2}|E_q(t)|^2+F_{N_q}.\end{aligned} \tag{2}$$

Here, $E_q(t) = r_q(t)e^{i\phi_q(t)}$ is the complex optical field and $N_q(t)$ the carrier number for the q-th laser. All remaining parameters coincide with those listed in the main text and Supplementary Tables 1 and 3. The noise terms take the following form. The complex term F_{E_q} represents spontaneous emission noise, modeled as Gaussian white noise with correlation

$$\langle F_{E_q}(t)F^*_{E_{q'}}(t')\rangle = R_{sp}\delta_{qq'}\delta(t-t').$$

The real-valued term F_{N_q} models carrier-number fluctuations and satisfies

$$\langle F_{N_q}(t)F_{N_{q'}}(t')\rangle = \gamma_n N_q(t)\delta_{qq'}\delta(t-t'),$$

consistent with Refs. [5–7].

The robustness of the pulsing state under these noise sources is illustrated in Supplementary Fig. 9. Supplementary Fig. 9(a) presents the intensity time series for a stable single-pulse solution in the 30-laser array for a feedback strength of $\kappa^f = 44.8\,ns^{-1}$

in the noise-free case. When the noise radius R_{sp} is gradually increased while keeping all other parameters fixed, the pulsing solution remains stable up to $R_{sp} = 0.1$, as shown in Supplementary Fig. 9(b).

A similar analysis performed for the two-laser configuration is shown in Supplementary Figs. 9(c) and 9(d). In this case, the pulsing state exhibits substantially greater robustness, persisting up to a noise radius of $R_{sp} = 10$.

These results demonstrate that coherent pulsing is highly resilient to realistic levels of spontaneous-emission and carrier-number noise, supporting the feasibility of observing the proposed dynamics in experimental semiconductor laser arrays.

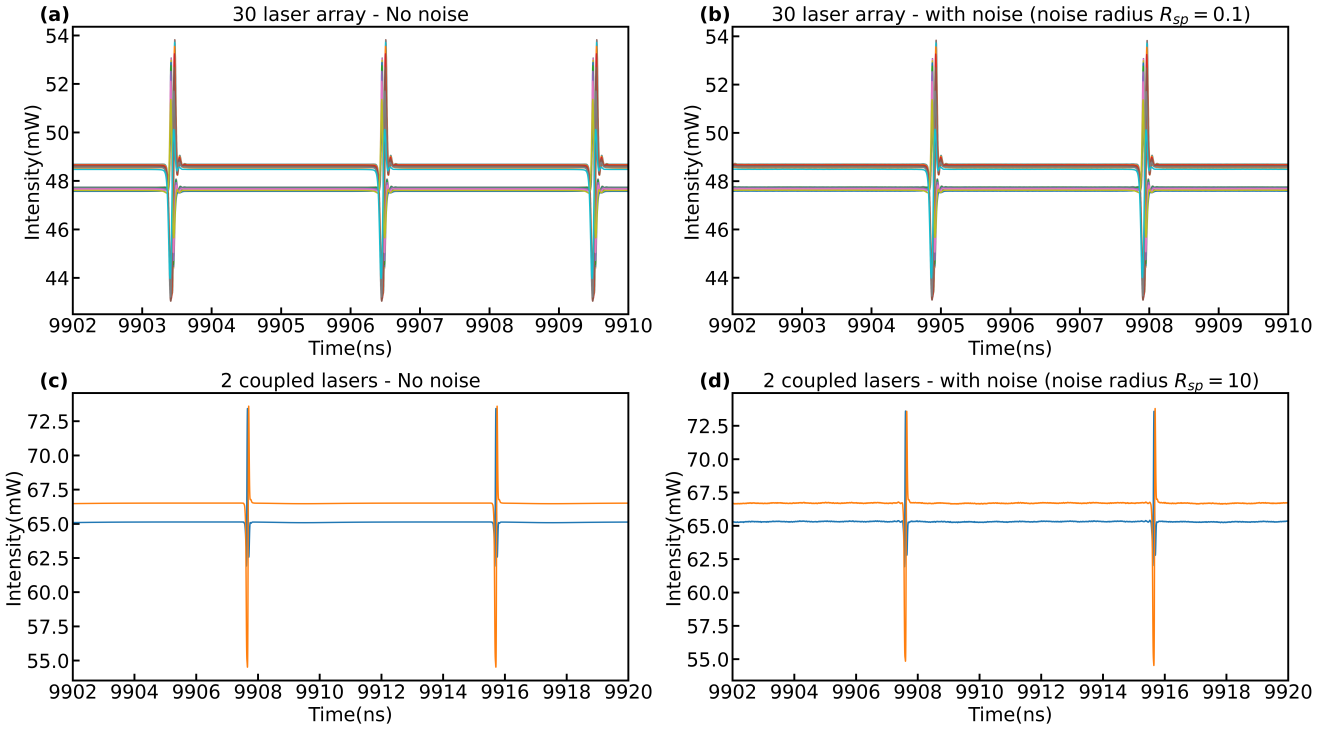

Supplementary figure 9. Robustness of pulsing dynamics to noise in both a 30-laser array and a two-laser system. (a) Intensity time series of the 30-laser array without noise at a feedback strength of $\kappa^f = 44.8$ ns^{-1}, illustrating stable single-pulse dynamics. (b) The same configuration with added noise ($R_{sp} = 0.1$), showing persistence of pulsing. (c) and (d) Intensity time series for the two-laser system with $\Delta\omega = 2.5$ GHz and $\kappa^f = 17$ ns^{-1} in the absence and presence of noise ($R_{sp} = 10$), respectively. In both systems, the pulsing state remains stable across a wide range of noise levels, confirming strong robustness to spontaneous emission noise.

Computational support for deriving the reduced model

The objective of the reduced model is to explain the origin of pulsing behavior in the minimum network required to generate it, namely, a network of two lasers with transverse coupling. The parameters used in the two-laser model shown in Fig. 4(a) of the main text are summarized in Supplementary Tab. 3. To derive the reduced model, we approximate $r_1(t-\tau) \approx r_1(t) \approx r_2(t-\tau) \approx r_2(t)$, $\phi_i(t-\tau) \approx \phi_i(t)$, and $N_1(t-\tau) \approx N_1(t) \approx N_2(t-\tau) \approx N_2(t)$. To demonstrate the validity of these approximations for the two-laser case, example plots are shown in Supplementary Fig. 10 for the pulsing case in which $\kappa^f = 18.0ns^{-1}$ and $\Delta\omega = 3.0GHz$.

The normalized differences between the non-delayed and time-delayed versions of $r_2(t)$, $\phi_2(t)$, and $N_2(t)$ are plotted in Supplementary Fig. 10(a). The absolute value of $(\phi_2(t) - \phi_2(t-\tau))/\phi_2(t)$ is below 5×10^{-5} for all time, and remains below 1.2×10^{-5} between pulses. The absolute value of $(N_2(t) - N_2(t-\tau))/N_2(t)$ is below 0.02 for all time and remains below 2×10^{-6} between pulses. The absolute value of $(r_2(t) - r_2(t-\tau))/r_2(t)$ is slightly larger, at a maximum around 0.2, but remains below 1×10^{-5} between pulses. This maximum value may be due to a period that differs slightly from τ or small differences in pulse shapes. The fact that all these values remain around zero for most of the time supports the approximations $r_2(t-\tau) \approx r_2(t)$, $\phi_2(t-\tau) \approx \phi_2(t)$, and $N_2(t-\tau) \approx N_2(t)$. The same trends hold true for laser 1, so $r_1(t-\tau) \approx r_1(t)$, $\phi_1(t-\tau) \approx \phi_1(t)$, and $N_1(t-\tau) \approx N_1(t)$.

Supplementary table 3. Details of the parameters for simulating the two-Lang-Kobayashi laser model array.

Symbol	Description	Value
λ	Wavelength	770 nm
α	Linewidth enhancement factor	2.5
g	Differential gain coefficient	1.5×10^{-5} ns^{-1}
s	Gain saturation coefficient	2×10^{-7}
γ	Cavity loss	500 ns^{-1}
N_0	Carrier number at transparency	1.5×10^{8}
γ_n	Carrier loss rate	0.5 ns^{-1}
ω_1	Frequency detuning for laser 1	-$\Delta\omega/2$
ω_2	Frequency detuning for laser 2	$\Delta\omega/2$
τ	Feedback delay time	8 ns
κ^f	Feedback strength	varied
d	Cross-laser reinjection efficiency	1.0
β	Pump factor	9.0
I_{th}	Threshold pump current for a single laser	14.7 mA

The normalized differences between the $r_i(t)$ and $N_i(t)$ values for the two lasers are shown in Supplementary Fig. 10(b). The absolute value of $(N_2(t)-N_1(t))/N_2(t)$ is below 0.025 for all time, and remains below 4.1×10^{-3} between pulses. The absolute value of $(r_2(t)-r_1(t))/r_2(t)$ is slightly larger, at a maximum under 0.2, but remains below 0.013 between pulses. As before, the fact these values are generally around zero validates the approximation $r_1(t)\approx r_2(t)$ and $N_1(t)\approx N_2(t)$.

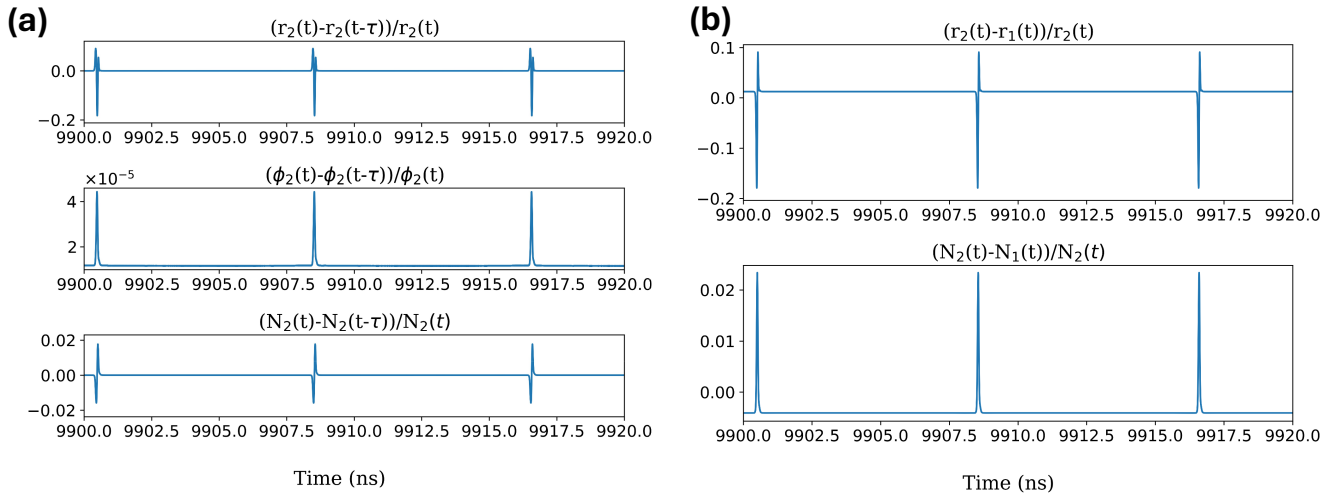

Supplementary figure 10. Plots demonstrating the validity of the approximations used for the reduced model. These are shown for the two-laser full Lang-Kobayashi model simulations for the pulsing case in which $\kappa^f = 18.0ns^{-1}$ and $\Delta\omega = 3.0GHz$. (a) normalized differences between non-delayed and time-delayed versions of $r_2(t)$, $\phi_2(t)$, and $N_2(t)$. (b) normalized differences between the $r_i(t)$ and $N_i(t)$ values for the different lasers.

Mechanism for pulse generation: pendulum analogy

To further elucidate the physical mechanism underlying the multi-pulse dynamics described by the phenomenological model (4), we draw an analogy with a driven, overdamped pendulum whose length varies periodically.

A schematic of this system is shown in Supplementary Fig. 12(a). The pendulum is subject to a constant external torque Γ and has a time-varying length given by $l(t) = L + A\cos\Omega t$. The kinetic and potential energies are given by $T = \frac{1}{2}m(\dot{l}^2 + l^2\dot{\theta}^2)$

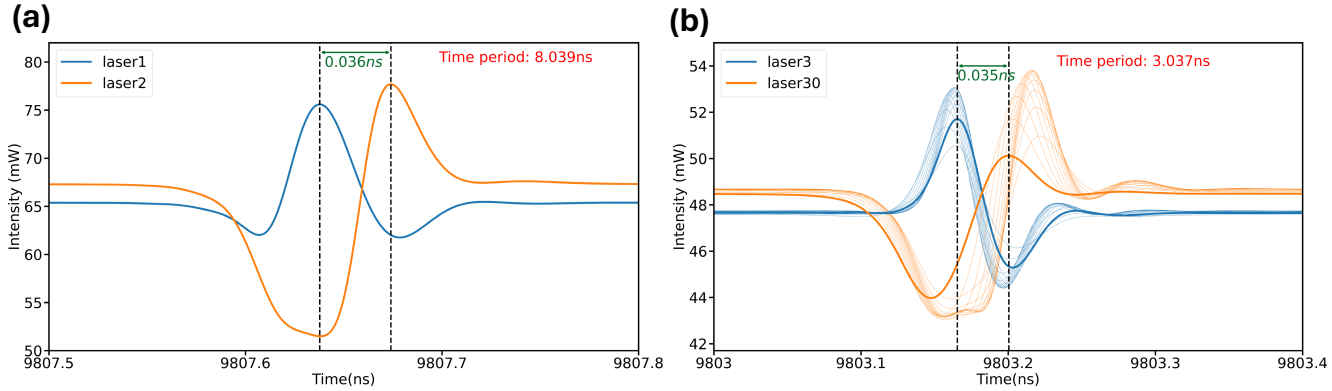

Supplementary figure 11. Time difference between the pulsing of the odd and even lasers. **(a)** Two coupled lasers: The time difference between the pulsing of the odd and even lasers is illustrated in the time series of intensities for two coupled lasers. The blue solid line represents the intensity of the first laser, while the orange solid line represents the intensity of the second laser. The black vertical dashed lines indicate the pulse timing for the first and second lasers. The time window between these pulses is approximately 0.036 ns. The total time period between pulsing events for the array is approximately 8.039 ns, slightly longer than the feedback delay time of $\tau = 8$ ns, indicating that the additional time unaccounted for, is approximately 0.039 ns. This is very close to the time difference between peaks in intensity for laser 1 and laser 2, as previously mentioned, 0.036 ns. The parameters are set as follows: $\Delta f = 3.5$ GHz, $\kappa^f = 19.5\text{ns}^{-1}$, with all other parameters as described in Supplementary Table 3. **(b)** 30 laser array: The odd and even groups are represented by blue and orange lines, respectively. Laser #3 and Laser #30 are depicted by bold lines. In terms of pulse timing, Laser #3 is the last laser in the odd group, while Laser #30 is the first laser in the even group. The time difference between the pulses of Laser #3 and Laser #30 is approximately 0.035 ns, which is very close to the additional time (≈ 0.037 ns) in the time period for this case. The parameters used are the same as those in Fig. 2(b) of the main text.

and $U = -mgl(t)\cos\theta$, respectively. The Lagrangian is then

$$\mathscr{L} = T - U = \frac{1}{2}m(\dot{l}^2 + l^2\dot{\theta}^2) + mgl(t)\cos\theta.$$

The equation of motion for the angular coordinate $\theta(t)$, incorporating damping and the applied torque, is derived from the Lagrange formalism:

$$ml^2\ddot{\theta} + 2ml\dot{l}\dot{\theta} + b\dot{\theta} + mgl\sin\theta = \Gamma,$$

where b is the damping coefficient.

In the overdamped regime, where $m^2gl^3 \ll b^2$, the inertial term can be neglected, leading to the simplified dynamics:

$$b\dot{\theta} + mgl\sin\theta = \Gamma.$$

By assuming $m = g = b = 1$ and substituting $l(t) = L + A\cos\Omega t$, we obtain:

$$\dot{\theta} = \Gamma - L(1 + a_1\cos\Omega t)\sin\theta,$$

where $a_1 = A/L$ quantifies the modulation amplitude. This equation is mathematically equivalent to the phenomenological model (Eq. (5) in the main text), thereby providing a physical analogue of the pulsation mechanism.

The dynamics of this system consist of long phases of slow angular evolution, during which it accumulates potential energy, punctuated by bursts of rapid rotation when the energy threshold is crossed, mimicking the pulsing behavior observed in the laser array. To visualize this, Supplementary Fig. 12(b) shows the potential energy $U(t)$ during the steady-state phase preceding bursts, with different curves corresponding to configurations producing one to seven pulses per period (achieved by varying a_1). As the number of pulses increases, the potential energy dip becomes more pronounced, indicating deeper energy accumulation.

In Supplementary Fig. 12(c), the number of pulses per period is plotted against the minimum of the potential energy preceding the burst. The apparent linear trend confirms that the depth of the energy well is a good predictor of the number of pulses emitted. These results support the interpretation of multi-pulse generation as an energy-accumulation-release process driven by the time-varying effective potential.

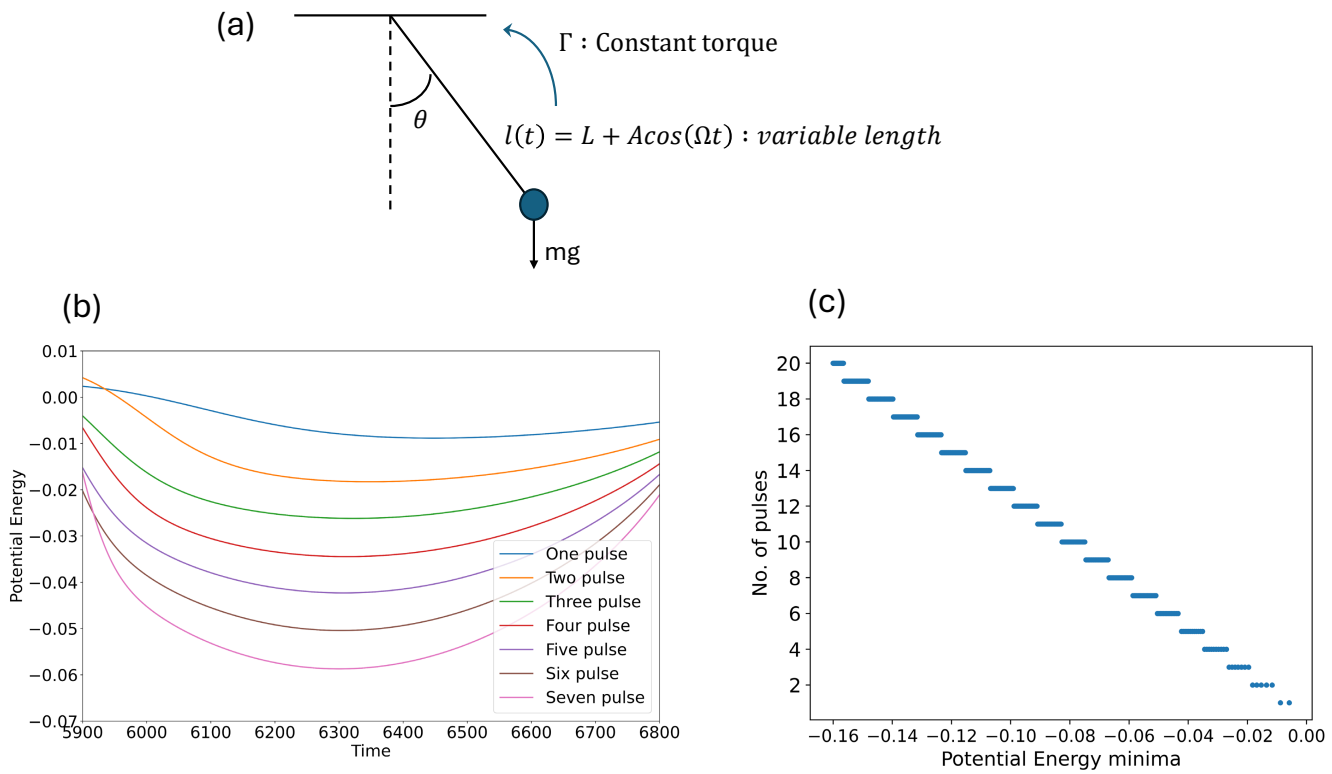

Supplementary figure 12. Pendulum analogy for pulse generation. (a) Schematic of an overdamped pendulum with time-dependent length $l(t) = L + A\cos\Omega t$, driven by a constant torque Γ. (b) Time series of potential energy $U(t)$ corresponding to pulsing regimes with one to seven pulses per period, obtained for different values of a_1. Larger a_1 values lead to deeper potential wells and higher pulse counts. (c) Number of pulses per period plotted versus the minimum potential energy before pulsing. The linear relationship confirms that deeper energy wells enable more pulses per cycle, reflecting the accumulation-release mechanism underlying the dynamics.

Supplementary References

1. Masoller, C. Spatiotemporal dynamics in the coherence collapsed regime of semiconductor lasers with optical feedback. Chaos: An Interdisciplinary Journal of Nonlinear Science 7, 455–462 (1997).
2. Dong, J.-X. Ruan, J. Zhang, L. Zhuang, J.-P. & Chan, S.-C. Stable-unstable switching dynamics in semiconductor lasers with external cavities. Physical Review A 103, 053524 (2021).
3. Liu, B. Braiman, Y. Nair, N. Lu, Y. Guo, Y. Colet, P. & Wardlaw, M. Nonlinear dynamics and synchronization of an array of single mode laser diodes in external cavity subject to current modulation. Optics Communications 324, 301–310 (2014).
4. Nair, N. Hu, K. Berrill, M. Wiesenfeld, K. & Braiman, Y. Using disorder to overcome disorder: A mechanism for frequency and phase synchronization of diode laser arrays. Physical Review Letters 127, 173901 (2021).
5. Koyu, S., Spitz, O., Berrill, M. & Braiman, Y. Dynamics and phase-locking in large heterogeneous arrays of semiconductor diode lasers. *High-Power Diode Laser Technology XXI*. **12403** pp. 199-215 (2023)
6. Soriano, M., Berkvens, T., Sande, G., Verschaffelt, G., Danckaert, J. & Fischer, I. Interplay of current noise and delayed optical feedback on the dynamics of semiconductor lasers. *IEEE Journal Of Quantum Electronics*. **47**, 368-374 (2011)
7. Yousefi, M., Lenstra, D. & Vemuri, G. Carrier inversion noise has important influence on the dynamics of a semiconductor laser. *IEEE Journal Of Selected Topics In Quantum Electronics*. **10**, 955-960 (2004)